

The Effect of the Mach Number on a Turbulent Backward-Facing Step Flow

Istvan Bolgar¹ · Sven Scharnowski¹ ·
Christian J. Kähler¹

Received: 15 November 2017 / Accepted: 10 April 2018 / Published online: 25 April 2018
© Springer Science+Business Media B.V., part of Springer Nature 2018

Abstract The flow around a backward-facing step in the sub-, trans- and supersonic regimes was investigated at the Trisonic Wind Tunnel Munich with particle image velocimetry and dynamic pressure measurements. These two techniques were combined to simultaneously measure and correlate the velocity fluctuations in a streamwise vertical plane with the pressure fluctuations on the reattachment surface. The results show that the dynamic loads on the reattachment surface increase from subsonic up to the transonic regime while the mean reattachment location moves downstream. As soon as the flow becomes locally supersonic aft of the backward-facing step, the mean reattachment location suddenly moves upstream while the normalized dynamic loads drastically decrease. By correlating the velocity and the dynamic pressure data, it was shown that a clear separation between outer flow and the flow close to the surface aft of the step is responsible for the drastic load reduction. Due to the large difference in pressure/density, the disturbances from the locally supersonic flow do not have an effect on the flow close to the surface. This is also reflected in the power spectral densities of the pressure fluctuations on the surface, showing that at supersonic free-stream Mach numbers a low-frequency pumping motion of the locally subsonic flow is the dominant mode, while in sub-/transonic flow Kelvin-Helmholtz instabilities and a cross-pumping motion of the shear layer dominate the dynamic loads.

Keywords Backward-facing step (BFS) · Flow separation · Subsonic · Transonic · Supersonic · Coherent flow structures · Particle image velocimetry (PIV) · Dynamic pressure measurements

✉ Istvan Bolgar
istvan.bolgar@unibw.de

¹ Institute of Fluid Mechanics and Aerodynamics, Bundeswehr University Munich, Neubiberg, Germany

1 Introduction

A flow around a backward-facing step (BFS) has been of scientific interest for decades for various reasons. For one, it provides a well-defined location for the onset of flow separation and thereby a shear layer with reattachment around a simple geometry. Therefore, phenomena regarding the flow separation, including the generation and amplification of flow disturbances, the reattachment thereof, and shear layer dynamics, can be studied in detail with such a simple shape. Another reason is that today the flow physics of the wake aft of a BFS, such as the modes responsible for the load fluctuations, have still not been fully understood [1]. This poses a problem for today's space launchers such as the Ariane 5 for example [2], which have a geometric discontinuity at the end of their main stage ahead of the cryogenic engine, similar to a BFS. By reattaching onto the nozzle of the main engine with strong local fluctuations, the turbulent separated shear layer causes high pressure fluctuations in the vicinity of the nozzle. This can result in the excitement of structural modes of the main engine's nozzle, a phenomenon referred to as buffeting [3], which can cause catastrophic structural damage. Since a space launcher travels through all Mach regimes during its trajectory, it is important to investigate the BFS flow at a series of different Mach numbers throughout the different regimes.

At subsonic velocities, experiments in the past have shown that the mean reattachment location varies between $5h - 8h$ [4], with h being the step height. This large deviation can partly be attributed to the fact that reattachment is sensitive to the pressure gradient present in the test section, altering the reattachment location by as much as $\pm 1h$ [5]. Also the near-wall turbulence level in the boundary layer has a considerable effect on the reattachment length. Increasing the turbulence level from 10 to 12.5% has been shown to reduce the reattachment length by as much as 25% [6].

Looking at the temporal behavior of a turbulent shear layer behind a BFS, the entire region of reverse flow fluctuates with several modes. Starting with the development of the linearly unstable shear layer, a high-frequency mode referred to as the 'shear layer mode', is found close to the step with a normalized frequency or Strouhal number of around $Sr_{\delta_2} \approx 0.012$ with respect to the momentum thickness δ_2 [7, 8]. It is caused by the periodic generation of Kelvin-Helmholtz instabilities present in all types of shear layers [9]. As the vortices created by the instabilities grow and move downstream, the pairing of vortices in three-dimensional space leads to a decrease in the frequency [7, 8]. This trend was also observed by Eaton and Johnston [10] who reported a rapid decay in the frequencies with increasing distance towards the reattachment location. Thus, close to reattachment a mode occurring at a lower frequency is often referred to as the 'vortex shedding mode' or 'step mode'. In literature, this mode has been reported over a wide spectrum, ranging from Strouhal numbers between $Sr_{L_r} \approx 0.6 - 1.0$ with respect to the reattachment length L_r [8, 11–13]. Underneath this spanwise vortex street, the recirculation zone exhibits its own dynamics. A low-frequency mode here is classically referred to as 'flapping', occurring between a Strouhal number of $Sr_h \approx 0.01 - 0.015$ with respect to the step height [1, 14], or $Sr_{L_r} \approx 0.1$ [11, 14]. As its name indicates, this mode causes a periodic change in the reattachment location by the flapping motion of the shear layer. A high-frequency 'pumping' mode within the recirculation zone also exists, where the reattachment location is relatively steady while the recirculation region pumps at $Sr_h \approx 0.07$ around the mean reattachment location [1]. Statnikov et al. also showed that these two modes exhibit a large periodic motion into the spanwise direction with a dominant wavelength of around two step heights, thus renaming these modes as 'cross-flapping' and 'cross-pumping'. Note that pumping in

that work refers to the classically called flapping and vice versa. However, the authors of this manuscript will use the classical notation throughout this manuscript.

Previously, the existence of large-scale periodic coherent structures with a length of several step heights and a wavelength of roughly two step heights that form shortly aft of the step had been shown by Scharnowski et al. [15, 16]. These structures strongly resemble the shape of the low-frequency cross-flapping mode as seen in [1]. One should also not mistake these large-scale coherent structures for time-averaged streamwise vortices that have been shown to appear in sub- [17, 18] and supersonic [19] wakes of BFS, as the structures found by Scharnowski et al. appear consistently over time, however randomly in space. When the velocity fields are time-averaged, there are no structures or streamwise vortices of any kind present, but the flow field is completely two-dimensional apart from side wall effects.

The instantaneous large-scale structures have also been found to appear in a very similar fashion on axisymmetric BFS models [20]. However, not only are the structures comparable between a planar and an axisymmetric model but also the major relevant parameters such as the shear layer instability and its growth rate [21]. Therefore, it can be assumed that there is a strong similarity between the driving mechanisms of a planar and an axisymmetric BFS flow, making a planar BFS relevant for research on the aft body aerodynamics of space launchers, for example. Furthermore, a planar model offers the advantages that the model is not suspended into the test section via a sword mount or a sting, thus allowing measurements without additional aerodynamic influences.

A major research aim of this work is to analyze the wake topology and its characteristics throughout all Mach regimes. Furthermore, the question arises what mechanisms cause the most dominant pressure loads on the reattachment surface. Previous research on supersonic BFS has shown that this flow is characterized by a much shorter reattachment for both, the planar as well as the axisymmetric cases [22, 23], than in the sub-/transonic regimes. Therefore, it is evident that when moving from the sub-/transonic into the supersonic regime, a large change in the flow physics is taking place, which is part of the current research focus.

2 Experimental Set-up

2.1 The test facility

All experiments were conducted at the Trisonic Wind Tunnel Munich (TWM) at the Bundeswehr University, which is a two-throat blow-down type wind tunnel with an operating total pressure range of 1.2 – 5 bar and a Mach number range of 0.15 – 3.00. Figure 1 shows some of the key features of this measurement facility. Up to 20 bar (above ambient) of pressurized dry air is stored in two tanks (2), holding a total volume of 356 m³. Typically, the air is a few Kelvin above ambient temperature after the tanks have been pressurized by up to three compressors (1). The test section (6) is 300 mm wide and 675 mm high with suction capabilities at both, the horizontal and the vertical walls. The vertical walls are fitted with suction holes, while the horizontal walls have suction slits. Both use the lower pressure available downstream in the diffuser (7) as their source of passive suction. The test section is surrounded by a plenum chamber that can be opened for easy access to the model. Once the plenum is closed, the gate valve can be opened and the pressurized air is released up to the control valve (4). When in operation, the control valve keeps a steady total pressure in the test via a closed loop control logic. By setting a desired total pressure, the Reynolds number can be varied between $(4 - 80) \times 10^6 \text{ m}^{-1}$. The Mach number in the test section

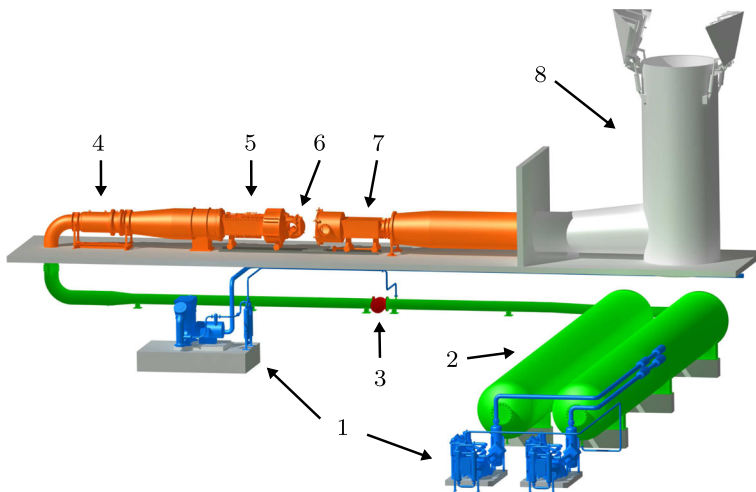


Fig. 1 Trisonic Wind Tunnel Munich: (1) compressors, (2) tanks, (3) gate valve, (4) control valve, (5) variable Laval nozzle, (6) test section, (7) variable diffuser/nozzle, (8) exhaust tower

is controlled by a variable diffuser/nozzle (7) downstream of the test section up until sonic conditions. Above this, a variable Laval nozzle (5) can also be adjusted in order to reach supersonic conditions. Both, the diffuser as well as the Laval nozzle can be adjusted steplessly with infinite increments. The Laval nozzle always takes the shape of an ideal contour nozzle, providing uniform flow above sonic conditions. Downstream of the diffuser the air is released into the atmosphere through the exhaust tower (8).

For the experiments under investigation, the side wall suction was taken advantage of below sonic conditions. This not only helps in reducing the low momentum boundary layers on the side walls of the test section, but also reduces blockage effects at transonic conditions. The horizontal walls' suction was not applied, as the light sheet for particle image velocimetry (PIV) was inserted at an angle from a top window inside the plenum. Slits in the horizontal walls equalize the pressure in the test section with the plenum when the horizontal walls' suction is not in use. However, when it is used, the pressure is reduced resulting in a pressure difference between the test section and the plenum. This would cause the light sheet to diffract due to the difference in the densities, thus changing the location of the illuminated domain with respect to the calibrated plane. However, in order to offset the increasing displacement thickness of the boundary layers on the horizontal walls and to get a rather small pressure gradient in the test section, the horizontal walls were put at a deflection angle, increasing the cross section in the direction of the flow by 25 mm over the test section length of 1.8 m.

2.2 Test cases & BFS model

Free-stream Mach numbers ranging from 0.3 up to 2.7 were examined over a BFS model. The free-stream turbulence levels for the experiments measured with PIV were between 1.2 – 2.3%, while decreasing with increasing free-stream Mach numbers. These numbers were obtained by taking the root mean square (RMS) of the fluctuations of the x - and y -components of the velocity at the upper left boundary of the PIV field of view (FOV) and

dividing them by the local mean velocity. Due to the measurement location and the uncertainty of PIV the real turbulence level is expected to be slightly lower. Table 1 provides the experimental conditions that were analyzed with PIV, dynamic pressure sensors, combined PIV/pressure measurements, and schlieren. The \pm values in the table indicate the standard deviation of each quantity during the measurements.

The quasi-2D generic space launcher model is symmetric about its horizontal plane and spans across the entire test section. It has a 150 mm long gently curved nose which smoothly transitions into a 105 mm long flat plate prior to the step. This shape was carefully designed in order to ensure local subsonic conditions (at $Ma_\infty = 0.8$) about the model’s forebody [20]. The step is 7.5 mm high on both sides and attaches to a 150 mm long splitter plate. The overall model’s thickness is 25 mm, while the step height to step width ratio is 1 : 40, providing an unaffected recirculation region due to side wall effects, according to [24].

On one side the splitter plate is fitted with 24 dynamic pressure sensors (Kulite XCQ-062 with a gauge pressure range of ± 3.5 bar) in the center of the model, aligned in parallel to the streamwise direction. They extend starting from $x/h = 0.5$ up to $x/h = 12$ with a constant spacing of $0.5h$. For reference purposes the model was also fitted with 24 static pressure ports (Pressure Systems DTC ESP-32HD) in the same streamwise locations as the dynamic pressure ports, however offset by 36 mm into the spanwise direction. Figure 2 shows essential details of the BFS model.

2.3 Particle image velocimetry

For the statistical analysis of the flow field in a streamwise FOV, instantaneous flow fields were computed with PIV. For this a Quantel EverGreen double pulse laser with 200 mJ per

Table 1 Free-stream flow conditions of TWM with the standard deviations of the quantities

Exp. method	Ma_∞	p_0 [bar]	p_∞ [bar]	T_0 [K]
PIV	0.30 ± 0.0015	1.20 ± 0.0013	1.131 ± 0.0012	294 ± 1.8
	0.50 ± 0.0013	1.20 ± 0.0019	1.012 ± 0.0015	292 ± 1.6
	0.80 ± 0.0008	1.73 ± 0.0017	1.129 ± 0.0012	291 ± 1.2
	0.90 ± 0.0006	1.60 ± 0.0016	0.943 ± 0.0009	290 ± 1.0
	2.00 ± 0.0010	2.20 ± 0.0023	0.282 ± 0.0004	292 ± 1.6
Pressure measurements	0.30 ± 0.0013	1.20 ± 0.0016	1.130 ± 0.0015	289 ± 1.0
	0.40 ± 0.0012	1.20 ± 0.0012	1.076 ± 0.0011	287 ± 0.9
	0.50 ± 0.0010	1.20 ± 0.0009	1.007 ± 0.0007	287 ± 0.9
	0.60 ± 0.0007	1.20 ± 0.0007	0.940 ± 0.0006	286 ± 0.8
	0.70 ± 0.0006	1.20 ± 0.0010	0.863 ± 0.0009	286 ± 0.8
	0.80 ± 0.0007	1.72 ± 0.0014	1.128 ± 0.0005	284 ± 0.6
	0.90 ± 0.0006	1.60 ± 0.0010	0.946 ± 0.0007	285 ± 0.7
	2.00 ± 0.0013	2.20 ± 0.0017	0.284 ± 0.0005	285 ± 0.7
Combined PIV/pressure	0.80 ± 0.0007	1.73 ± 0.0013	1.129 ± 0.0010	285 ± 1.0
	2.00 ± 0.0012	2.20 ± 0.0014	0.283 ± 0.0005	286 ± 1.3
Schlieren	0.80 ± 0.0007	1.73 ± 0.0015	1.129 ± 0.0007	285 ± 0.7
	0.90 ± 0.0007	1.60 ± 0.0012	0.942 ± 0.0007	287 ± 0.7
	2.00 ± 0.0009	2.20 ± 0.0015	0.283 ± 0.0006	286 ± 0.7

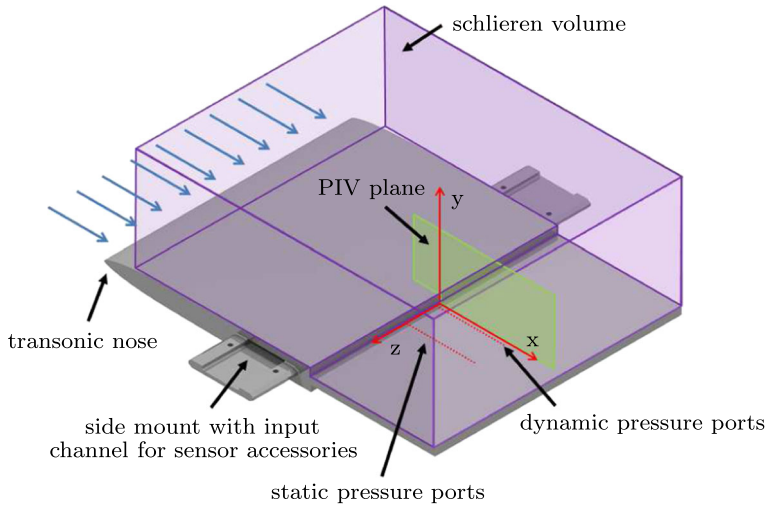


Fig. 2 Illustration of the planar space launcher model with its pressure ports and the field of view under investigation

pulse illuminated Di-Ethyl-Hexyl-Sebacat (DEHS) tracer particles with a mean diameter of $1\ \mu\text{m}$ [25], which were added just downstream of the control valve of the wind tunnel. The particles were imaged onto a 2560×2160 pixel sensor of a LaVision Imager sCMOS camera with a 50 mm planar objective lens from Zeiss. The PIV system's trigger events were controlled by a LaVision PTU X. For each of the Mach numbers listed in Table 1, at least 1000 double images with a statistically independent frequency of 15 Hz were recorded. The time separation between an image pair was between $0.8 - 4.5\ \mu\text{s}$ depending on the free-stream Mach number, limiting the particle image shift to about 10 – 15 pixel in the outer flow. This ensures that the error due to curved streamlines and spatial gradients, which lead to loss-of-correlation due to out-of-plane motion, is sufficiently low [26, 27].

The data processing consisted of a pre-processing step, the PIV evaluation itself, and a post-processing step. The pre-processing step was comprised of an image shift correction in order to compensate for camera vibrations, and subtracting the background reflections by means of proper orthogonal decomposition (POD) [28]. Instantaneous PIV images, used for statistical analyses such as the two-point correlations, had a final interrogation window size of 12×12 pixel with 50 percent overlap, yielding a vector grid spacing of $210\ \mu\text{m}$. The interrogation windows included a Gaussian window weighting and image deformation from LaVision DaVis 8.3. The mean flow fields were then obtained by averaging the instantaneous vector fields. In order to determine the state of the incoming boundary layer ahead of separation, a single-pixel ensemble-correlation method with symmetric double correlations [29] was applied to obtain a spatially highly resolved mean flow field [30] upstream of the BFS.

2.4 Dynamic pressure measurements

In addition to the PIV measurements, dynamic pressure measurements were also conducted. These measurements were not only carried out for the same Mach numbers as PIV, but also for various other Mach numbers for a more complete overview (refer to Table 1). The

24 dynamic sensors were sampled simultaneously with a frequency of 25.6 kHz, gathering 128,000 samples in 5 s for each Mach number while static pressure ports were sampled with 200 Hz. Both, the static and dynamic pressure ports were given a reference pressure from the free-stream at $x/h \approx -30$, hence measuring the difference to the static pressure in the test section’s free-stream. The dynamic pressure transducers were calibrated simultaneously by applying various relative pressures within the range of ± 0.8 bar onto the backside of the membranes via reference tubes with a General Electric PACE 5000 pressure controller, and measuring their voltages. This resulted in a calibration curve for each sensor. After calibration, the unfiltered mean values of the dynamic sensors were compared to the static values and showed a near perfect match (refer to Fig. 3). Thus, the results summarized in Section 3.6 show only the pressures gathered with the dynamic sensors. Figure 3 also shows the standard deviations of the pressures measured with the static and the dynamic sensors. As is to be expected, the static sensors underestimate the dynamics significantly since their signals are dampened by the viscous effects in the long pressure lines. Note that the dynamic pressure sensors at $x/h = 3.5, 6.5$ & 10 were not used for the measurements, as some of the 24 available electrical ports were used to also measure pressure fluctuations in the free-stream and ahead of the step simultaneously.

2.5 Combined PIV/Pressure measurements

For the scope of this manuscript, PIV and dynamic pressure were measured simultaneously for a trans- ($Ma_\infty = 0.8$) and a supersonic case ($Ma_\infty = 2.0$). This was done in order to compare a flow with subsonic behavior aft of the step (without supersonic expansion around the BFS) while being close to sonic conditions, to a flow with supersonic behavior aft of the step (with supersonic expansion around the BFS) that has stable measurement conditions while still being reliable for statistical analysis using PIV. At both of the free-stream Mach numbers, 500 PIV images were recorded at 15 Hz while recording the dynamic pressure data at 25.6 kHz, gathering just above 850,000 pressure samples at each port. By measuring PIV simultaneously to the pressure at various locations, it is possible to correlate the velocity

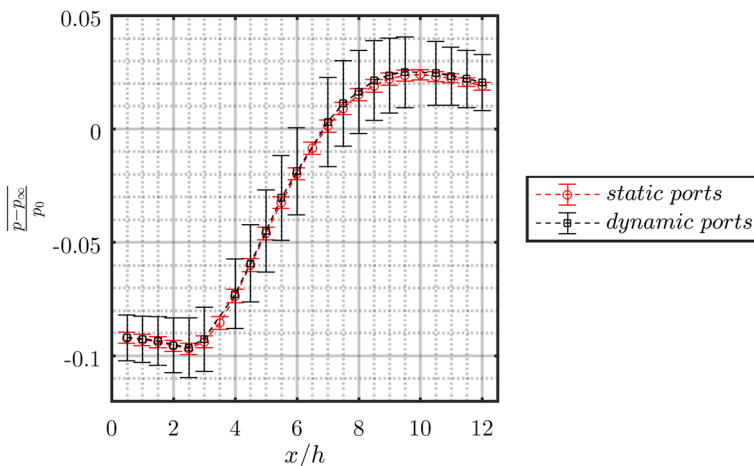


Fig. 3 Comparison of the mean total pressure coefficients measured with static pressure probes vs. dynamic pressure transducers at $Ma_\infty = 0.8$. The error bars indicate the standard deviations of the pressures

fluctuations to the pressure fluctuations [31–34]. This technique makes it possible to visualize the fluid structures that cause the dominant pressure loads on the surface in a spatially highly resolved velocity plane. The triggering event of the PIV system and the pressure sensors was set up to work simultaneously so that each vector field can be assigned to a certain pressure sample at each sensor. When the 500 corresponding pressure signals are correlated to their 500 velocity fields, the pressure fluctuations at one pressure port have been correlated to a component of the velocity fluctuations in the 2D velocity plane, as described by Pearson’s correlation coefficient in Eq. 1 [35].

$$R_{pu}(x, y) = \frac{\sum_{i=1}^N [p_i(x_0) - \bar{p}(x_0)][u_i(x, y) - \bar{u}(x, y)]}{\sqrt{\sum_{i=1}^N [p_i(x_0) - \bar{p}(x_0)]^2 \sum_{i=1}^N [u_i(x, y) - \bar{u}(x, y)]^2}} \tag{1}$$

where the term $[p_i(x_0) - \bar{p}(x_0)]$ is the fluctuating portion of the pressure (or p') evaluated at a streamwise location x_0 , while the term $[u_i(x, y) - \bar{u}(x, y)]$ is the fluctuating portion of a scalar of the velocity vector (or u' or v' in this manuscript) evaluated in the entire 2D plane of the FOV. A pressure sample is evaluated with its corresponding image i up to the sum of all the images N .

The temporal resolution of PIV can be artificially improved by means of pressure transducers. For this, the pressure signals are shifted by t' and correlated to the vector fields. This means that a set of pressure signals recorded prior to- or after the double images were taken can show what is happening before and after in relation to the images. This allows for a statistical tracking of dominant phenomena over time with the temporal resolution of the dynamic pressure sensors, thus an artificially improved temporal resolution. Each correlation image shows the correlation between the 500 velocity fields to 500 pressure measurements with an offset of t' , as can be seen in Eq. 2.

$$R_{pu}(x, y, t) = \frac{\sum_{i=1}^N [p(x_0, t_i - t') - \bar{p}(x_0)][u_i(x, y) - \bar{u}(x, y)]}{\sqrt{\sum_{i=1}^N [p(x_0, t_i - t') - \bar{p}(x_0)]^2 \sum_{i=1}^N [u_i(x, y) - \bar{u}(x, y)]^2}} \tag{2}$$

where $(t_i - t')$ indicates that not only the PIV images’ corresponding pressure terms p' recorded at t_i can be correlated to the PIV images, but also pressure fluctuating terms offset by a certain time step t' .

2.6 Schlieren measurements

For further qualitative analyses, a two color schlieren system (from four available colors) was used, which allows the visualization of density gradients, isentropic compression and expansion waves, and compressible shear layers. The light source of the schlieren system installed in the TWM is a 1.6 kW xenon lamp, from which spectrum’ the colors red and green were extracted via band-pass filters. The two colors were overlapped with a 2-sided prism mirror. A bi-condenser projected each of the two colors onto their own slit, where the slits for red and green were aligned in the vertical direction. The slits were placed in the focus of a concave mirror with a focal length of 4000 mm in a classical Z-setup, so that the light aft of the mirror traveled through the side windows of the test section in parallel. On the other side of the test section, the changes in the parallelism of the light were detected.

In order for this to work, the light was focused onto so-called knife edges with a second concave mirror before being projected onto a camera sensor. For a detailed description of the schlieren system installed at the TWM facility, the reader is referred to [36]. In order to complement the PIV measurements, the two transonic free-stream Mach numbers ($Ma_\infty = 0.8$ & $Ma_\infty = 0.9$) as well as the supersonic free-stream Mach number ($Ma_\infty = 2.0$) were measured with the schlieren system, visualizing the density gradients in the horizontal direction. Table 1 summarizes the wind tunnel conditions. Figure 4 shows the shock free design of the nose at $Ma_\infty = 0.8$, while at $Ma_\infty = 0.9$ a nearly normal shock is present ahead of the step. It can also be seen in this figure that the reflected shock at $Ma_\infty = 2.0$ does not interfere with the measurement domain for PIV or the pressure ports, as it gets reflected past the bounds of the schlieren image. At $Ma_\infty = 0.9$ an expansion is also visible in the black zone about the step. This indicates that the flow accelerates aft of the normal shock to just above sonic conditions, which is in agreement with the PIV data as well as the Mach number distribution in the test section shown in Section 3.2. The two lambda shocks, one forming ahead of the step and the other one forming due to reattachment, are both stable in time. This is also the case for bow shock and the recompression shock at $Ma_\infty = 2.0$.

3 Results and Discussion

3.1 Incoming boundary layer

The incoming boundary layer was evaluated at $x/h = -1$ using single-pixel ensemble-correlation as described in Section 2.3. This allowed for a spatial resolution of $35 \mu\text{m}$ per vector in the wall-normal direction, while the first reliable vector is at $\approx 100 \mu\text{m}$ due to wall reflections and loss of seeding. The rest of the boundary layer was extrapolated linearly towards the wall, allowing to estimate the upper limits of the displacement and momentum thickness. The boundary layer parameters of the thickness δ_{99} , the displacement thickness δ_1 , momentum thickness δ_2 , the shape factor H_{12} , and the momentum thickness Reynolds number for the various Mach numbers are listed in Table 2. For all investigated Mach numbers, the incoming boundary layers were turbulent according to [37], as the shape factor H_{12} is around 1.4. As the densities in the boundary layer are not known, the displacement thickness was determined by using the incompressible definition for all cases:

$$\frac{\delta_1}{h} = \frac{1}{h} \int_1^\infty \left[1 - \frac{\langle u(y) \rangle}{\langle u(\delta_{99}) \rangle} \right] dy \tag{3}$$

Similarly, the incompressible definition for the momentum thickness was used:

$$\frac{\delta_2}{h} = \frac{1}{h} \int_1^\infty \frac{\langle u(y) \rangle}{\langle u(\delta_{99}) \rangle} \left[1 - \frac{\langle u(y) \rangle}{\langle u(\delta_{99}) \rangle} \right] dy \tag{4}$$

The shape factor H_{12} was then determined by the ratio of the two:

$$H_{12} = \frac{\delta_1}{\delta_2} \tag{5}$$

3.2 Mach number distribution in the test section

Figure 5 shows the local Mach number along the test section measured on the bottom wall and referenced with a static pressure probe at $x/h \approx -30$ (for the standard deviations of

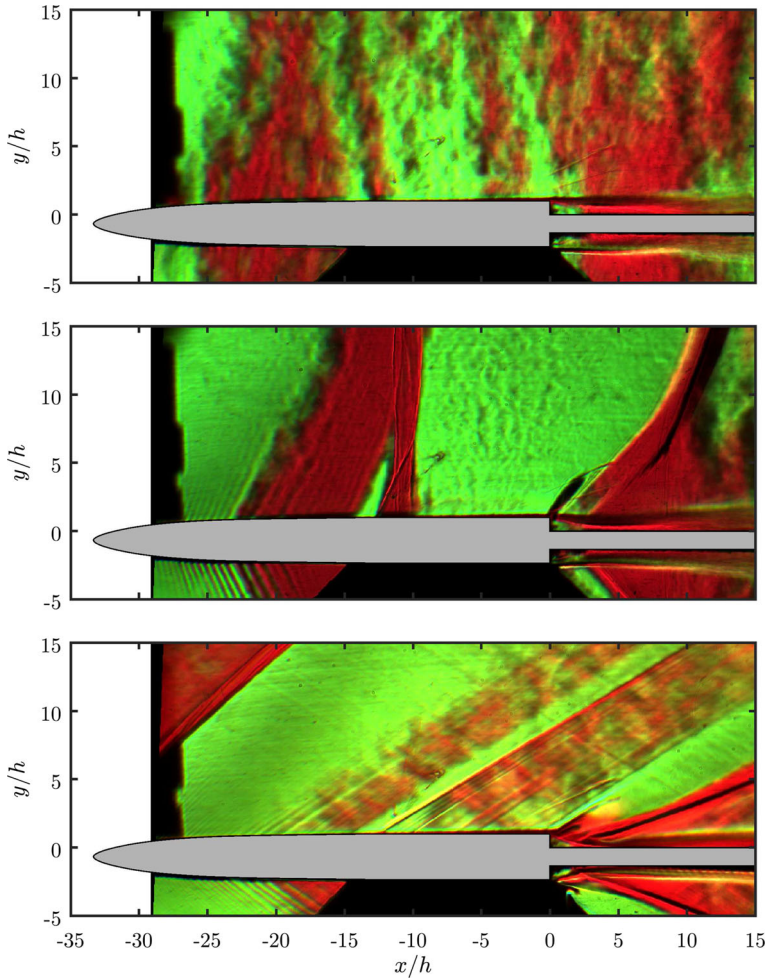


Fig. 4 Instantaneous schlieren recordings showing the density gradients in the horizontal direction at $Ma_\infty = 0.8, 0.9, \& 2.0$ from top to bottom. Red to green corresponds to increasing density in the streamwise direction while green to red corresponds to decreasing density

the Mach number refer to Table 1). Right away, the free-stream Mach numbers 2.0 & 2.7 distinguish themselves from the other free-stream Mach numbers, while $Ma_\infty = 0.9$ is also a lot different than the other runs.

Table 2 Incoming boundary layer parameters at $x/h = -1$

Ma_∞	U_∞ [$\frac{m}{s}$]	$\frac{\delta_{99}}{h}$	$\frac{\delta_1}{h}$	$\frac{\delta_2}{h}$	H_{12}	Re_{δ_2}	Re_h
0.30	≈ 102	0.40	< 0.061	< 0.045	≈ 1.36	≈ 2600	$\approx 58,000$
0.50	≈ 167	0.37	< 0.062	< 0.041	≈ 1.53	≈ 3700	$\approx 90,000$
0.80	≈ 258	0.35	< 0.057	< 0.041	≈ 1.39	≈ 7400	$\approx 180,000$
0.90	≈ 285	0.34	< 0.053	< 0.035	≈ 1.53	≈ 6200	$\approx 177,000$
2.00	≈ 511	0.47	< 0.056	< 0.038	≈ 1.49	≈ 7900	$\approx 208,000$

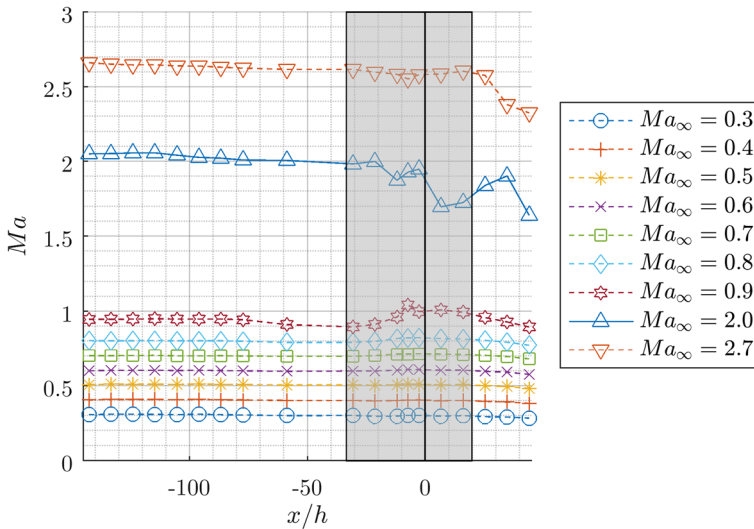


Fig. 5 Mach number distribution within the test section referenced to a static pressure probe at $x/h \approx -30$

For the $Ma_\infty = 2.0$ case, the sudden drop in the Mach number at $x_{wall}/h \approx -20$ is due to a separated shock forming in front of the model’s nose, which reaches the horizontal walls ahead of $x_{wall}/h \approx -12$. At this point the shock has already lost intensity and is rather a Mach wave, which is reflected back towards the center of the test section. Due to an acceleration over the model’s nose followed by a compression fan where the nose’s curvature reduces, the Mach number first increases from $x_{wall}/h \approx -12$ till $x_{wall}/h \approx -2.5$ and then decreases strongly till $x_{wall}/h \approx 7$. At this point the effect of the expansion fan around the step can be noticed till $x_{wall}/h \approx 35$, as the Mach number on the wall rises. Finally, the oblique shock stemming from the recompression through reattachment causes the lastly portrayed Mach number drop along the horizontal walls. A similar trend can be seen for the $Ma_\infty = 2.7$ case, however with much lower Mach number changes as the angle of the oblique/reflected shock and expansion waves are much steeper, thus reducing their intensities. It can also be seen that the final Mach number drop occurs earlier at $x_{wall}/h \approx 16$. Note that the Mach number changes along the wall can be seen further downstream as they occur on the model, due to the angles of the compression/expansion waves, thus the location of impact on the Mach number changes. It can be summarized that for the supersonic cases the Mach number distribution in the test section is as expected and of good quality, as the Mach number changes created by the model do not affect the measurement domain itself while the reflected shock from the wind tunnel wall does not interfere with the measurement domain either.

At $Ma_\infty = 0.9$ the presence of the model induces a Mach number drop in the test section upstream of itself from $x_{wall}/h \approx -87$ to $x_{wall}/h \approx -30$. From there on the expansion over the nose’s curvature can be seen till $x_{wall}/h \approx -7$. At that point the Mach number suddenly drops again till $x_{wall}/h \approx -2.5$. This is due to the formation of a nearly normal shock as a result of the compression waves meeting, which are created by the decreasing curvature, as illustrated in the schlieren image (refer to Fig. 4 in the middle). Therefore, the definition of the free-stream Mach number $Ma_\infty = 0.9$ should be viewed with caution, as blockage occurs around the model. Thus, the Mach number aft of the shock, just ahead of the step,

is higher than the free-stream Mach number referenced at $x/h \approx -30$. By means of PIV it was determined to be $Ma \approx 1.00 \pm 0.01$ at $x/h = -1$. After the shock, the flow then expands through an expansion fan around the BFS till $x_{\text{wall}}/h \approx 7$, from where the oblique recompression shock/fan creates a drop in the wind tunnel wall Mach number till the end of the test section. Again, this can be seen nicely in the schlieren image in Fig. 4. In order to be able to compare the pressure dynamics downstream of the step between the various free-stream Mach numbers, the values were normalized with the total pressure, which again is set/defined further upstream of the model. As the normal shock on the model surface creates a loss in the total pressure, the pressure ratios provided in Section 3.6.1 at $Ma_\infty = 0.9$ are slightly smaller than those of lower Mach numbers, as they were divided by the total pressure ahead of the model/normal shock.

At $Ma_\infty = 0.8$ a slight expansion from the flow accelerating over the model's nose can be noticed without a stationary shock (refer to Fig. 4 on top), while all other subsonic free-stream Mach numbers show a gradient of nearly a zero in the Mach number distribution.

3.3 Tracer particle response across recompression shock

For the $Ma_\infty = 0.9$ and 2.0 cases measured with PIV, a recompression shock forms on the reattachment surface, as the locally sonic flow gets deflected into a parallel direction with respect to the reattachment surface. It is known that the tracer particles do not decelerate suddenly, such as the discontinuity due to a shock would suggest, but rather that they need a certain distance and time for adjusting to the local flow conditions [38]. This lag can be quantified by the relaxation distance ξ_p and time τ_p . For both, the $Ma_\infty = 0.9$ and 2.0 cases $\xi_p \approx 0.6$ mm while $\tau_p \approx 1.9$ μ s. These values are nearly identical with previous findings on DEHS tracer particles [39]. Furthermore, as the interrogation window sizes are smaller than the relaxation distance, while the separation time between two frames is on the order of the relaxation time, the analysis thereof can be considered reliable [39] apart from a small region around the shock (≈ 1 vector). As a result, the velocity fields approximately portray the reality ahead and aft of the shocks, while the shocks themselves are shown with a width of ξ_p on the PIV images.

3.4 Mean flow field & reattachment

Looking at the mean flow fields in Fig. 6, it becomes evident that with increasing Mach numbers reattachment moves downstream, at least up to $Ma_\infty = 0.8$. As soon as the flow is locally above sonic conditions ahead of the step (from $Ma_\infty = 0.9$), a supersonic expansion occurs around the step forcing reattachment to move upstream again. With a further increase in Mach number, the expansion angle around the step gets steeper, therefore further decreasing the reattachment length. The overall large deviation in the reattachment length for varying Mach numbers is characteristic of the planar BFS, while being present in a weaker manner on axisymmetric BFS. Due to the radial degree of freedom the axisymmetric case provides, mean reattachment occurs further upstream in general. Above sonic conditions, either configuration's mean reattachment length is controlled by the Prandtl-Meyer expansion around the step, purely a function of the Mach number. The trend either configuration shows at various Mach numbers is similar and provides another similarity next to the nature of the three-dimensional large-scale structures and the shear layer instability/growth rate mentioned in Section 1. Figure 7 compares the reattachments from the experiments of this manuscript with other experimental reattachment locations on axisymmetric BFS. The mean reattachment locations were determined by taking the first reliable vector above

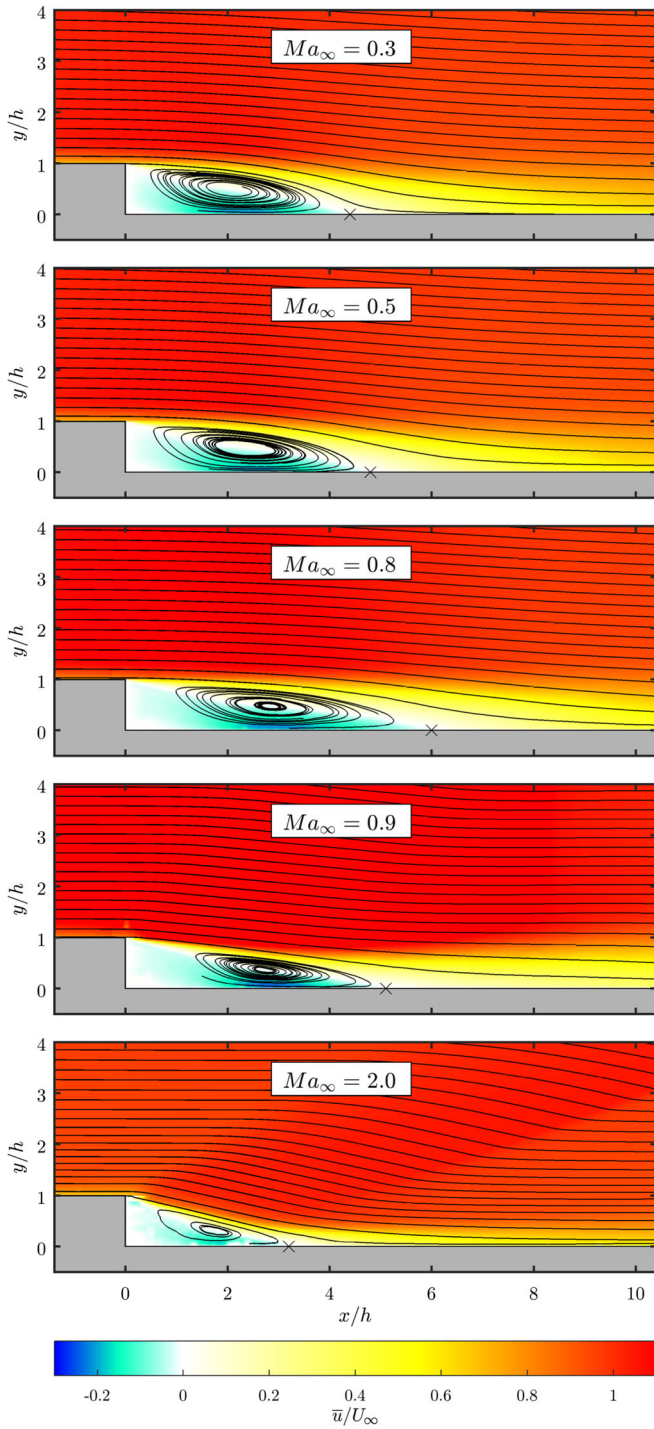


Fig. 6 Streamwise component of the mean flow fields at various Mach numbers

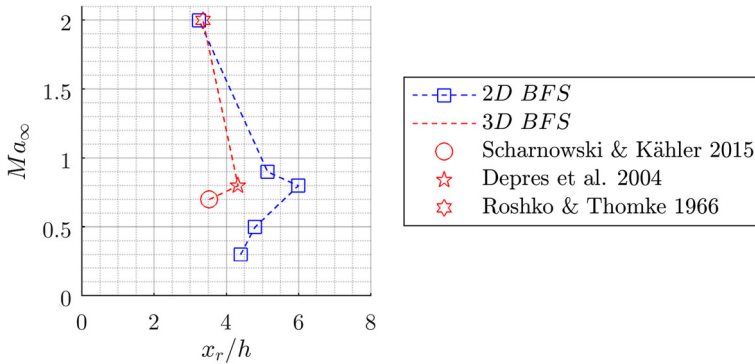


Fig. 7 Free-stream Mach number vs. reattachment length for planar and axisymmetric BFS: $Ma_\infty = 0.7$ from [40], $Ma_\infty = 0.8$ from [41], $Ma_\infty = 2$ from [23]

the surface, whose x -component was positive. Since the mean reattachment locations were determined using standard PIV as described in Section 2.3 and not single-pixel ensemble correlation, the first reliable vector above the surface was at $y/h = 0.028$ or $200 \mu\text{m}$ above the surface.

The subsonic flow fields are rather similar as can be seen from Fig. 6. It can also be noticed that the maximum of the mean horizontal component of the back-flow velocities are around -20% of the free-stream velocity, regardless of the Mach number. The maximum values of the mean horizontal component of the velocities are around 110% of the free-stream, until $Ma_\infty = 0.9$, where a supersonic expansion is already present around the step. The mean reattachment as well as the extrema values of both mean velocity components are summarized in Table 3.

3.5 Dynamic flow field statistics

Looking at the back-flow ratios in close proximity of the reattachment surface at various free-stream Mach numbers gives an idea of the spatio-temporal flow behavior (refer to Fig. 8). The figure shows the number of back-flow events normalized with the total number of measurements extracted from instantaneous PIV vector fields at a height of $y/h = 0.1$ as a function of the streamwise location. In the secondary recirculation region, there is little back-flow for all free-stream Mach numbers. The back-flow ratios increase to above 90% for all Mach numbers, reaching around 95% for $Ma_\infty = 0.8$ at $x/h = 2.65$. A back-flow ratio of 50% is reached just slightly ahead of the mean reattachment location, since it was

Table 3 Mean flow field statistics and extrema from PIV

Ma_∞	x_r/h	\bar{u}_{max}/U_∞	\bar{u}_{min}/U_∞	\bar{v}_{max}/U_∞	\bar{v}_{min}/U_∞
0.30	4.4	1.07	-0.21	0.05	-0.13
0.50	4.8	1.08	-0.21	0.04	-0.12
0.80	6.0	1.13	-0.22	0.05	-0.10
0.90	5.1	1.32	-0.24	0.31	-0.13
2.00	3.2	1.07	-0.18	0.16	-0.24

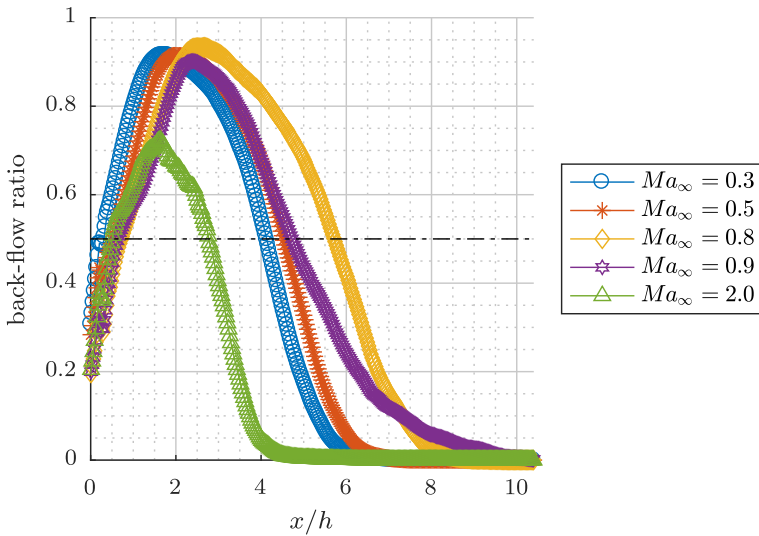


Fig. 8 Back-flow ratio for various Mach numbers at $y/h = 0.1$

determined just above the surface. This shows that around the reattachment location the flow has approximately the same amount of forward as reverse flow events. As the back-flow ratio shows the temporal behavior at the horizontal locations, the negative slope of the ratio indicates the steadiness of the flow. A highly negative slope after the maximum back-flow location means that reverse flow events quickly fade away with increasing distance aft of the step. Therefore, the case with the steadiest reattachment dynamics is the $Ma_\infty = 2.0$ case because it has the largest negative slope near reattachment. Its maximum back-flow ratio peaks around 75%, whereas all other free-stream Mach numbers' back-flow maxima are around 95%. $Ma_\infty = 0.9$ shows the least negative slope around reattachment, or most changes to the velocity directions at the respective streamwise locations. This behavior at a height of $y/h = 0.1$ reflects the results of the Reynolds shear stresses shown in Fig. 9, where at $Ma_\infty = 0.9$ the Reynolds shear stresses are relatively high close to the surface, when compared to the other free-stream Mach numbers. Thus, at this height above the surface the velocity fluctuations and the number of reverse flow events are very high, likely caused by the interaction of the recompression shock aft of reattachment with the shear layer.

At $Ma_\infty = 0.8$ the portion from $x/h = 2.5 - 5$ is also slightly less negative than the rest of the subsonic free-stream Mach numbers. Hence, the recirculation region shows a slightly more unstable behavior in the transonic regime than at regular subsonic conditions. This is most likely due to the stronger presence of the flapping mode in transonic conditions (refer to Section 3.6.3), causing a higher amount of momentum exchange with the flow outside of the shear layer.

The Reynolds shear stresses in Fig. 9 show the averaged velocity fluctuations taking place in the 2D flow fields, indicating the presence of turbulent vortical structures. From $Ma_\infty = 0.3 - 0.8$ the maxima of the absolute normalized intensities of the shear fluctuations stay about the same, reaching around 2.5% of the square of the free-stream velocity. However, one can notice how the area of the higher intensity fluctuations increases with increasing Mach number (up to $Ma_\infty = 0.8$), indicating a larger spread of vortices aft of the BFS. The intensity and spread majorly increases at $Ma_\infty = 0.9$, where the maximum of the

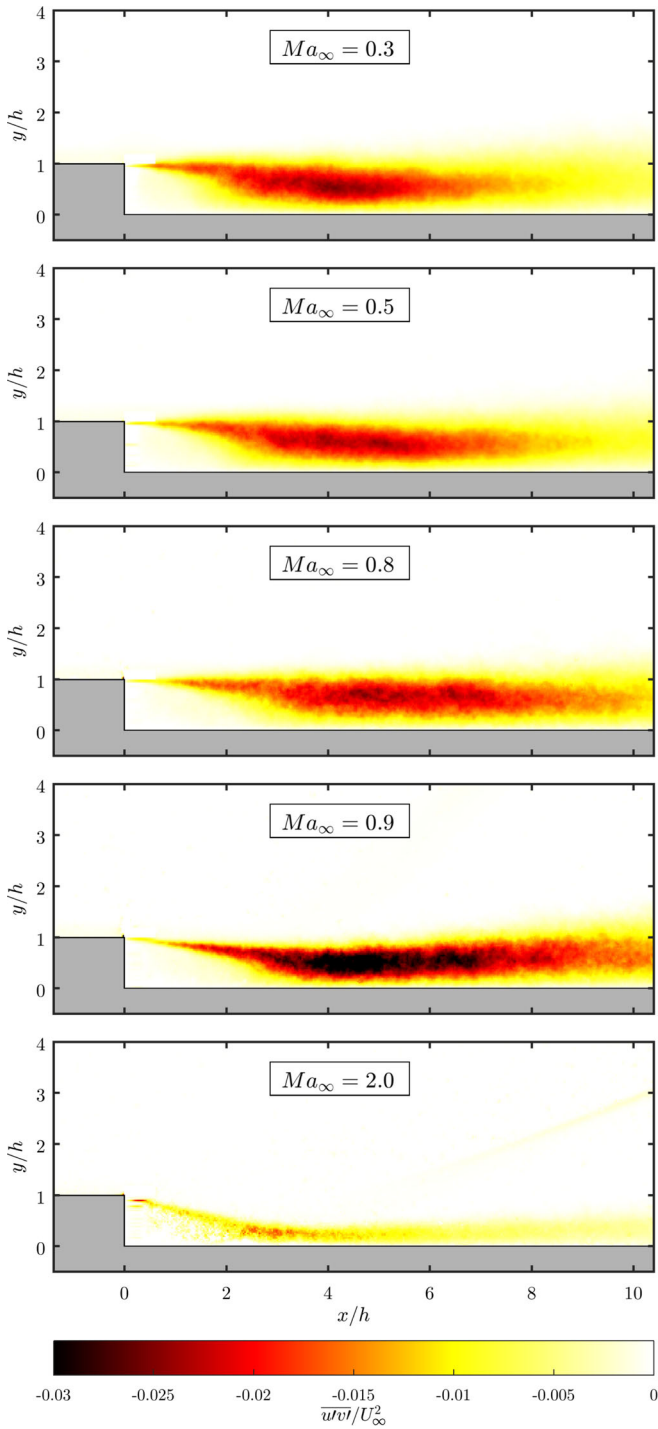


Fig. 9 Reynolds shear stresses at various Mach numbers

absolute mean intensity reaches 3.8% of the square of the free-stream velocity. These values should be viewed with caution though, as the values are normalized to the free-stream velocity, which is much lower than the velocity right ahead of the step. Regardless, the high intensities just outside of the recirculation region indicate that the formation of the lambda shock is strongly interacting with the shear layer, thereby causing large changes in velocity. In supersonic conditions at $Ma_\infty = 2.0$ the Reynolds shear stresses already decrease substantially in their normalized magnitude as well as their spreading. It becomes clear that the major velocity fluctuations occur in close proximity of the reattachment surface. This due to the fact that the region in between the supersonic expansion about the step and the oblique shock fan forming close to the reattachment location is very stable. This can be explained by the fact that both, the supersonic expansion as well as the oblique shock occur at defined angles, which are a function of the Mach number and the deflection angles imposed by the geometry. This is also the reason why the oblique shock seen in Fig. 4 is stable in time.

Figure 10 shows a line plot of the normalized Reynolds stresses at the reattachment locations of the various Mach numbers. From $Ma_\infty = 0.3 - 0.8$ it can be seen that the maxima of the absolute magnitudes decrease slightly while also moving further away from the reattachment surface, caused by the broadening of the shear layer. At $Ma_\infty = 0.9$ the absolute magnitudes (normalized by the defined free-stream velocity ahead of the model) reach their maxima and start moving back towards the reattachment surface. At $Ma_\infty = 2.0$ the maximum absolute magnitude of the Reynolds stresses moves closer to the reattachment surface again as the shear layer becomes thinner, while strongly weakening in its normalized magnitude, indicating a steadier flow field. The normalized intensities of the Reynolds stresses however, do not give an indication of the trend of the normalized pressure fluctuations on the surface (refer to Section 3.6.1) when comparing the various free-stream Mach numbers.

3.6 Dynamic pressure measurements

3.6.1 Mean pressure and RMS fluctuations on the reattachment surface

For comparison reasons, the reference pressure for the dynamic pressure measurements was selected to be just in front of the step up to $Ma_\infty = 0.9$ in order to compensate for the strong blockage present at the $Ma_\infty = 0.9$ case. The supersonic cases were referenced with a pressure port in front of the bow shock stemming off the model's nose. The pressure data was normalized by the total pressure instead of the dynamic pressure q_∞ (refer to Table 1). This allows for a direct comparison of the normalized pressure data at different Mach numbers, which would not be the case when normalizing with q_∞ , due to the large increase in the dynamic pressure with increasing Mach number. For simplicity, this quantity will be referred to as the total pressure coefficient C_{p0} .

Similarly, as would be expected with the pressure coefficient, the total pressure coefficient starts converging to a value of 0 towards the end of the reattachment surface (refer to Fig. 11 at the top). For the mean total pressure coefficient, there is systematic rise in the suction as well as in its pressure recovery with increasing Mach number below sonic conditions, as is expected. The supersonic cases show the weakest expansion and recoveries.

The root mean square (RMS) of the pressure fluctuations provide a good overview of the dynamic loads that occur on the reattachment surface. In Fig. 11 on the bottom, it can be seen that the average pressure fluctuations start to increase slowly with increasing Mach number from $Ma_\infty = 0.3 - 0.5$. At $Ma_\infty = 0.6$ the average pressure fluctuations increase drastically, while from $Ma_\infty = 0.7$ the high pressure fluctuations start to spread out, reaching the maximum overall intensities. At $Ma_\infty = 0.8$ the intensities slightly decrease,

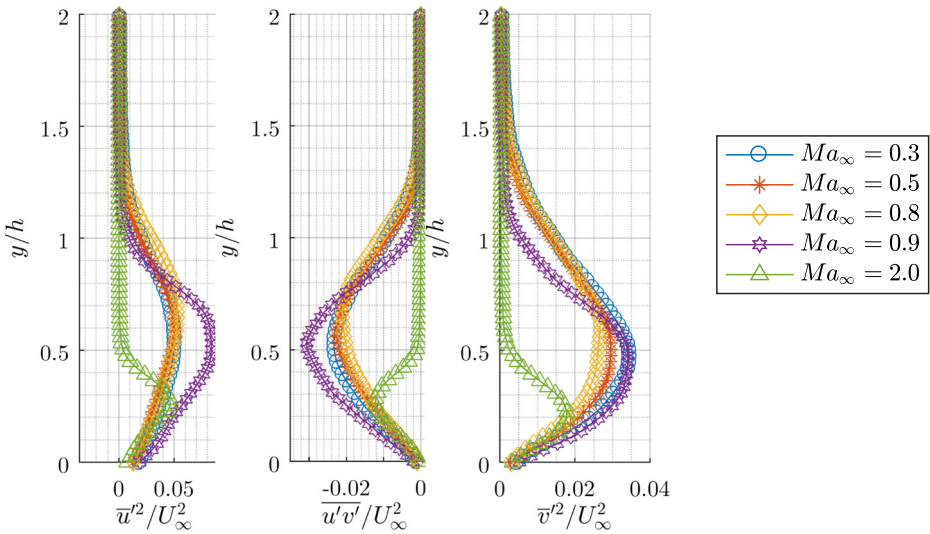


Fig. 10 Reynolds stress profiles at x_r for various Mach numbers

while at $Ma_\infty = 0.9$ and the supersonic cases the average pressure fluctuations drastically decrease with increasing Mach number. The maximum of the average pressure fluctuations occurs at approximately reattachment from $Ma_\infty = 0.3 - 0.5$. At $Ma_\infty = 0.8$ however, the maximum average pressure fluctuations move downstream to $x/h = 7$, whereas the reattachment occurs at $x/h = 6$. Overall it can be concluded that the reattachment surface experiences the highest mean loads in the transonic regime from $Ma_\infty = 0.6 - 0.8$. One should also note that the bending moment of the average loads is loosely coupled to the mean reattachment location, an important criterion in some engineering applications such as a space launcher. Thus, the most extreme bending moment dynamics occur between $Ma_\infty = 0.7 - 0.8$.

3.6.2 Pressure fluctuations in space and time

The behavior of the pressure fluctuations in space and time is shown in Fig. 12 for $Ma_\infty = 0.8$ and $Ma_\infty = 2.0$. Figure 12 shows 200 pressure samples over a time period of approximately 8 ms for each sensor. For the transonic case, one can track coherent structures moving downstream when looking at the diagonal patches, shown in either blue or red, moving towards the right top of the image. As the diagonal lines appear relatively often, the structures are occurring at quite a high and consistent frequency. In contrast, the supersonic case seems to have slightly less coherence, while the footprints of the pressure fluctuations are thicker and more widespread. Thus it seems that coherent eddies are not the cause of the load fluctuations on the surface in the supersonic regime, but rather a different mechanism of the subsonic layer close to the surface. This will be further elaborated on in Sections 3.7.1 and 3.7.2.

3.6.3 Pressure spectra

The pressure spectra provided in Fig. 13 show the power spectral density (PSD) over the length of the reattachment surface from $x/h = 0 - 12$ for the various free-stream Mach

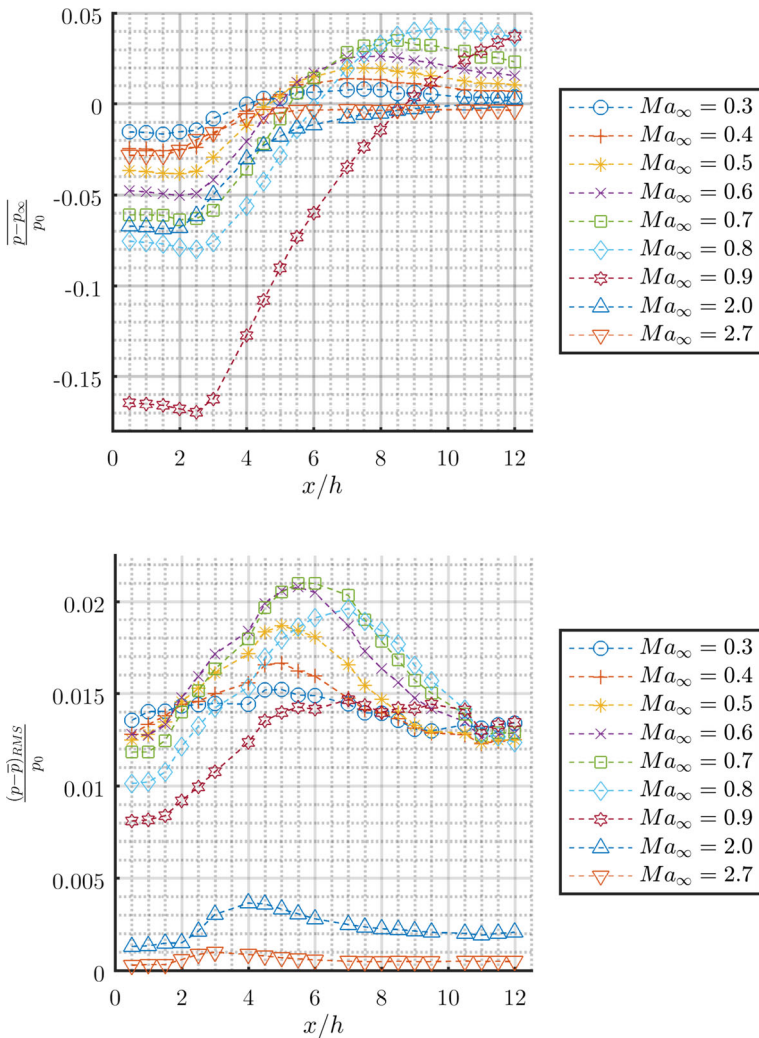


Fig. 11 Mean and root mean squared pressures at various Mach numbers

numbers. The power spectral density is given in units per Hertz, as the pressure fluctuations were normalized by the total pressure for each measurement, while its value is indicated by the intensity of the color. A plot for $Ma_\infty = 0.3$ is not provided, as the sensor sensitivity is not as accurate for low pressure fluctuations (refer to sensor pressure range in Section 2.2).

The dominant peaks spanning horizontally across the plots, shown in the dark colors (e.g. at $f \approx 400 \text{ Hz}, 1000 \text{ Hz}, 1800 \text{ Hz}$), are the wind tunnel background noise. This can be deduced by the fact that the frequencies stay consistent along the streamwise locations with increasing free-stream Mach numbers.

The dominant peaks in the spectrum increase in their frequency range (at approximately constant Strouhal number Sr_{L_s}) as well as in their normalized intensities from $Ma_\infty = 0.4 - 0.7$. This is consistent with the findings of the mean pressure fluctuations, as they also

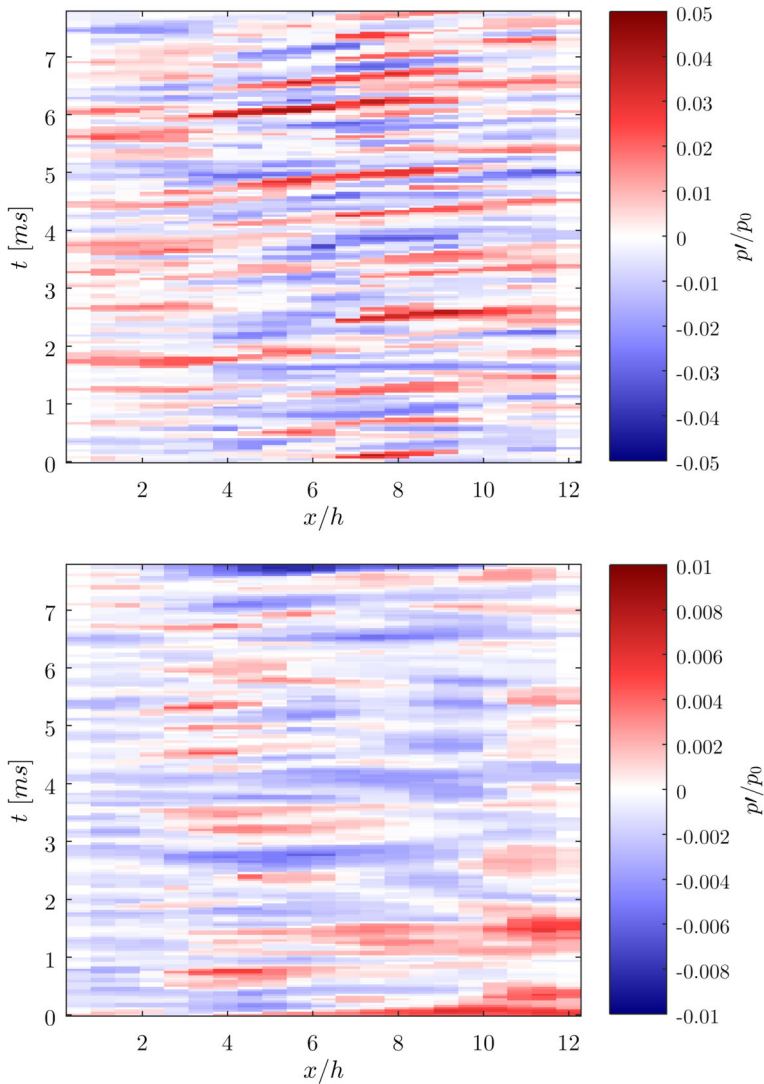


Fig. 12 Normalized pressure fluctuations at $Ma_\infty = 0.8$ (on top) and $Ma_\infty = 2.0$ (on bottom) in space and time

reach their maximum at $Ma_\infty = 0.7$. From $Ma_\infty = 0.9$ the normalized intensities strongly decrease and other patches start to appear.

Below sonic conditions, it can be said that there are various patches/broadband peaks or modes in the spectra, each being independent from the other one. Each mode decreases in its frequency while moving downstream, as seen in [10]. From $Ma_\infty = 0.4 - 0.6$ there are three clearly visible modes, each one being dominant at a different streamwise segment. From $Ma_\infty = 0.7 - 0.8$ however, the two rearwards modes merge together. Additionally a fourth distinct mode can be lightly seen around $x/h = 4 - 6$ below 1000 Hz from $Ma_\infty = 0.6 - 0.8$.

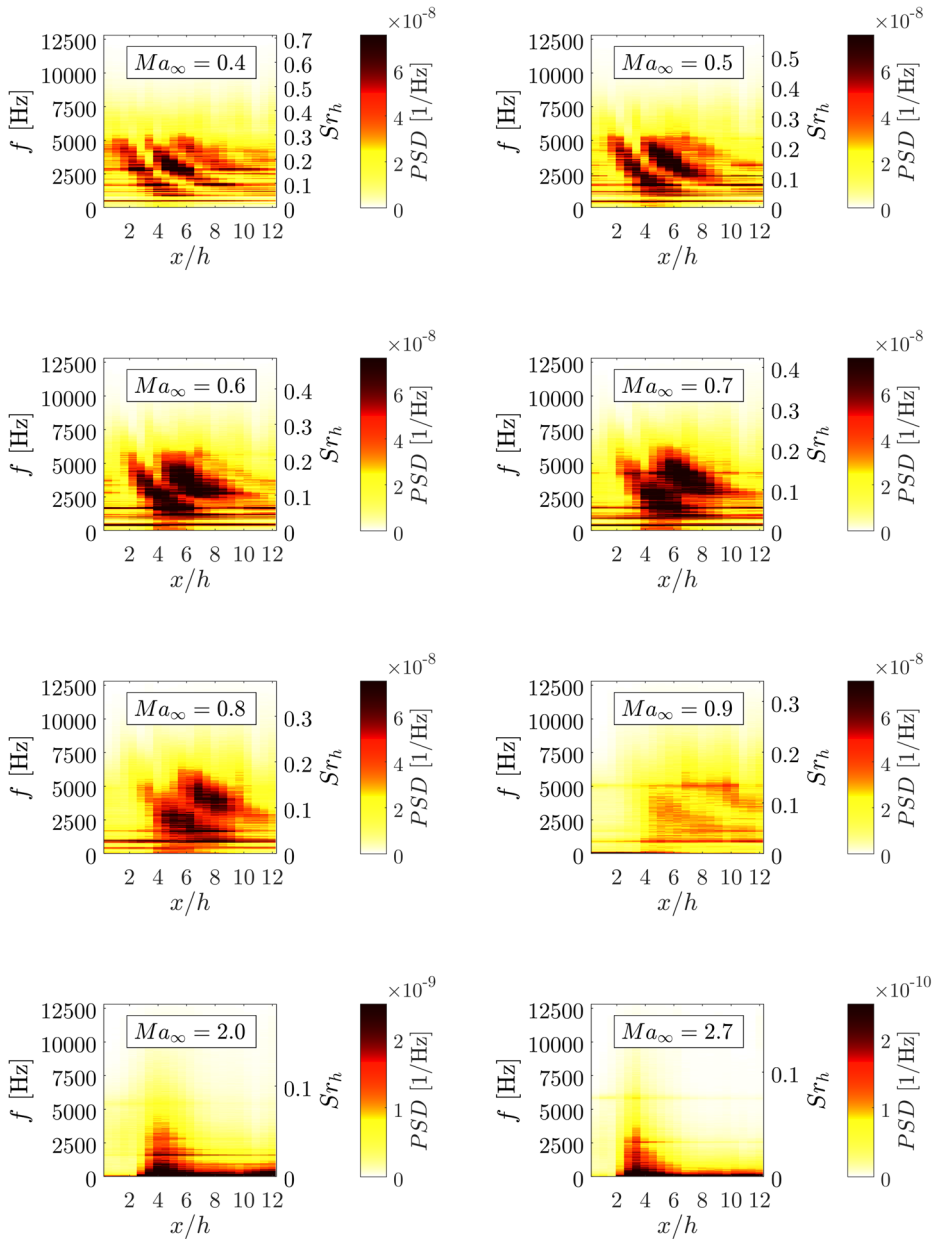


Fig. 13 Streamwise evolution of the power spectral density of the surface pressure fluctuations at various free-stream Mach numbers

The two major modes overlap right around the reattachment location, or the location of the highest mean pressure fluctuations. The mode closer to the step acts upon the recirculation region and exhibits Strouhal numbers typical for the cross-pumping mode of the shear layer, as described in [1]. The frequencies at the centers of the patches/modes are

slightly decreasing with increasing free-stream Mach numbers and can be found between Strouhal numbers of $Sr_{L_r} \approx 0.4 - 0.6$, similar to previous findings [1, 4, 42]. Thus, this mode can be characterized as the pumping or more recently discovered cross-pumping mode.

The more rearwards mode, having a Strouhal number of $Sr_{L_r} \approx 0.7$ at the centers of its patches, can be characterized as the step mode as defined by Hasan [8]. This mode's normalized frequency range falls right into values found previously in literature, ranging from $Sr_{L_r} = 0.6 - 1.0$ [8, 11–13]. The large spread in those results can now be explained by the fact that the dominant frequency of this mode decreases while moving downstream. This makes the dominant frequency of a PSD measured with one sensor very sensitive to its streamwise location. The step mode is dominated by Kelvin-Helmholtz vortices, which will be further verified in Section 3.7.1.

The decrease in the frequencies with increasing distance away from the step can be explained by the fact that the smaller scale structures start to grow together in three-dimensional space to combine larger ones while moving downstream. This theory is supported by the fact that the two major modes both have a continuous trend and can clearly be separated into distinct phenomena. This theory is in contrast to Hasan's opinion, who suggested that an intermittent upstream motion of the large-eddy structure is responsible for the decrease in the frequencies [8]. Furthermore, he based his theory on findings from Troutt et al. [43], who observed that pairing interactions were strongly inhibited in the reattachment region. When looking at the spectra around reattachment, it becomes clear that the nature of the problem is by far more complex, as two different modes act upon that location. However, when following the 'step mode' further downstream, the pairing of vortices is a very feasible explanation, while the decrease in the frequencies noticed in previous literature when moving upstream is in reality caused by another mode.

The centers of the weak mode below 1000 Hz between $x/h = 4 - 6$ from $Ma_\infty = 0.6 - 0.8$ are found at around $Sr_h \approx 0.01$, coinciding with the low-frequency cross-flapping mode described in [1]. In contrast to the other modes, this mode's dominant frequency slightly increases with increasing distance away from the step. This is very likely due to the fact that the structures causing the cross-flapping motion statistically occur more often further downstream, rather than a breakdown mechanism of the structures.

Looking at the spatial spectrum at $Ma_\infty = 0.9$, it becomes clear that a large change in the flow physics is taking place when the flow is locally sonic ahead of the step already. Suddenly, the intensity of both modes decreases drastically while moving further downstream. With a further increase in the free-stream Mach number to supersonic conditions, the two previously registered dominant modes do not show up on the surface pressure signatures anymore, while a broadband peak close to reattachment can be found above 1000 Hz as well as a widespread low-frequency patch below that. Due to the broadband peak's spatial location as well as its extremely broadband characteristic, the authors assume this to be a mode induced by the fluctuating recompression shock. Below 1000 Hz the strong low-frequency band spans from just ahead of the reattachment location all the way to the end of the measurement domain for both, $Ma_\infty = 2.0$ & 2.7 . Thus a low-frequency motion within the subsonic/boundary layer of the reattached flow becomes the dominant mechanism for the dynamic loads on the surface, as will be elaborated on in Section 3.7.2. This low-frequency mode is likely of the same nature as the low-frequency behavior found in other supersonic separated flows, which is probably caused by the dynamics of the separated bubble [44–46]. It is important to point out that this phenomenon extends all along the length of the reattachment surface and is not confined to the recirculation zone.

3.7 PIV/Pressure correlations

3.7.1 Subsonic correlations

When comparing the intensities of the pressure fluctuations in Fig. 11 on the bottom with the velocity fluctuations in Fig. 9 at different wind tunnel conditions, it becomes evident that their magnitudes do not correlate. The maximum normalized velocity fluctuations at reattachment for instance, occur at $Ma_\infty = 0.9$, showing high intensity fluctuations close to the surface. At that Mach number the pressure fluctuations are already quite low however. This indicates that the dynamic loads on the reattachment surface are not purely a function of the magnitude of the velocity fluctuations. In order to find a driving force for the dominant pressure loads on the reattachment surface, they were correlated with the velocity fluctuations in the 2D PIV plane.

When looking at the correlations at $Ma_\infty = 0.8$ in Fig. 14, it can be seen that the dominant flow structure causing the pressure fluctuations is in form of Kelvin-Helmholtz instabilities. This can especially be seen when correlating the y -component of the velocity fluctuations with the pressure fluctuations at $x/h = 7$, as seen in Fig. 14. When there is a positive pressure fluctuation p' at a certain streamwise sensor, the red color in the figure spatially indicates that it is accompanied by a positive velocity fluctuation v' , while the blue color indicates a negative velocity fluctuation $-v'$. Through the orientation of the

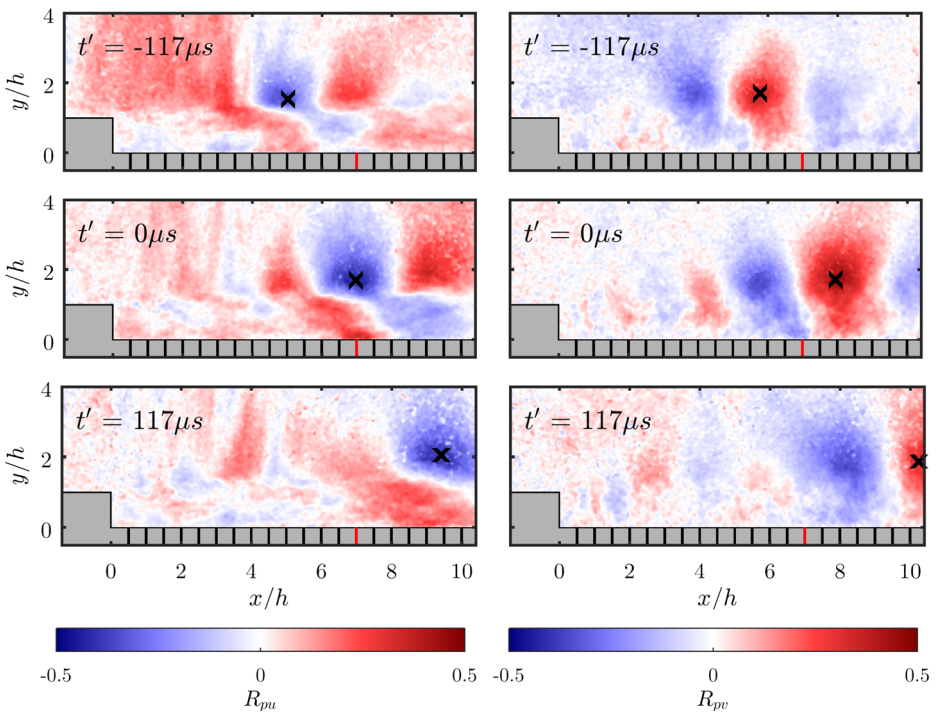


Fig. 14 Correlation of pressure fluctuations at $x/h = 7$ to the scalars of the velocity field fluctuations at $Ma_\infty = 0.8$. Left column shows R_{pu} , right column shows R_{pv} . Images from top to bottom are offset by two time steps of the pressure transducers or $t' = 117 \mu s$

scalars, one can easily imagine a circular motion across neighboring red and blue patches. As they occur periodically in space, spanwise vortices, or Kelvin-Helmholtz instabilities more precisely, can be deduced from the correlations.

At $t' = 0$ (left center image in Fig. 14) the correlation peak of R_{pu} , indicated by the red color, is right above the pressure transducer at $x/h = 7$. These findings are similar to the pressure velocity correlations by Hudy et al. [34] or the recently published work of Chovet et al. [33]. However, by having correlated the temporally offset pressure signals at $t' = -117 \mu s$ and at $t' = 117 \mu s$ (3 time steps before and after $t' = 0$) to the PIV images, one can statistically track the most dominant structures in space and time, as shown by the authors in [31]. This allows for the computation of the convection velocities, and with the given time steps, the frequencies of these dominant phenomena.

The most dominant frequency at $Ma_\infty = 0.8$ for instance, occurs around 4200 Hz ($Sr_h \approx 0.12$), according to the PIV/pressure correlations. This was also verified with the spectrum of the same sensor (located at $x/h = 7$), showing a broadband peak around the same frequency corresponding to the step mode. The cross-pumping mode found in the spatial spectrum (refer to Fig. 13) around 2400 Hz ($Sr_h \approx 0.07$) does not appear in the pressure-velocity correlations.

For the subsonic regime, it can be concluded that the Kelvin-Helmholtz vortices acting upon the reattachment surface in form of the step mode are the driving factor for the most dominant pressure fluctuations, which could also be deduced from Fig. 12. Even though they may be very three-dimensional in nature, statistically they clearly occur in a coherent way when displayed on a 2D plane, such as the FOV under investigation. For the future it would be interesting to investigate a streamwise horizontal FOV, to see whether the structures correlate with the finger-like structures in [16].

3.7.2 Supersonic correlations

In contrast to the subsonic case, the dominant pressure fluctuations occurring on the reattachment surface do not come from Kelvin-Helmholtz vortices in the supersonic case. When looking at the PIV/pressure correlations in Fig. 15, the pressure fluctuations strongly correlate with the x -component of the velocity fluctuations of the entire shear layer, indicating a pumping motion for the most dominant mode. The y -component of the velocity fluctuations has an apparent anti-correlation in the expansion area behind the step, while the shock correlates well with the pressure fluctuations. This indicates that the motion of the shock is coupled to the pressure fluctuations. Overall it is obvious that in the supersonic regime it is not the coherent structures from the shear layer that have an effect on the pressure fluctuations close to the surface. It seems that the entire streamwise shear layer movement, or pumping, causes the most dominant pressure loads. It could be inferred that there is a distinct separation between the outer region, or the supersonic flow, and the recirculation region/shear layer or newly developing boundary layer, or the subsonic flow. In other words, it almost seems that the supersonic flow is decoupled from the subsonic region in terms of the effects reaching the surface in the form of pressure fluctuations. In the PIV/pressure correlations this is indicated by the clear distinction of the colors as well as the recompression shock terminating at the subsonic layer assumed to be in red color (on the R_{pu} correlations in Fig. 15 on the left). This would indicate that the phenomena taking place in the outer regions do not protrude into the flow regions close to the surface, thus they do not have an effect on the wall pressure fluctuations. This could also be one of the reasons, why the normalized loads at $Ma_\infty = 2.0$ decrease by about an order of magnitude when comparing it to the loads at $Ma_\infty = 0.8$ (refer to the average pressure fluctuations in Fig. 11).

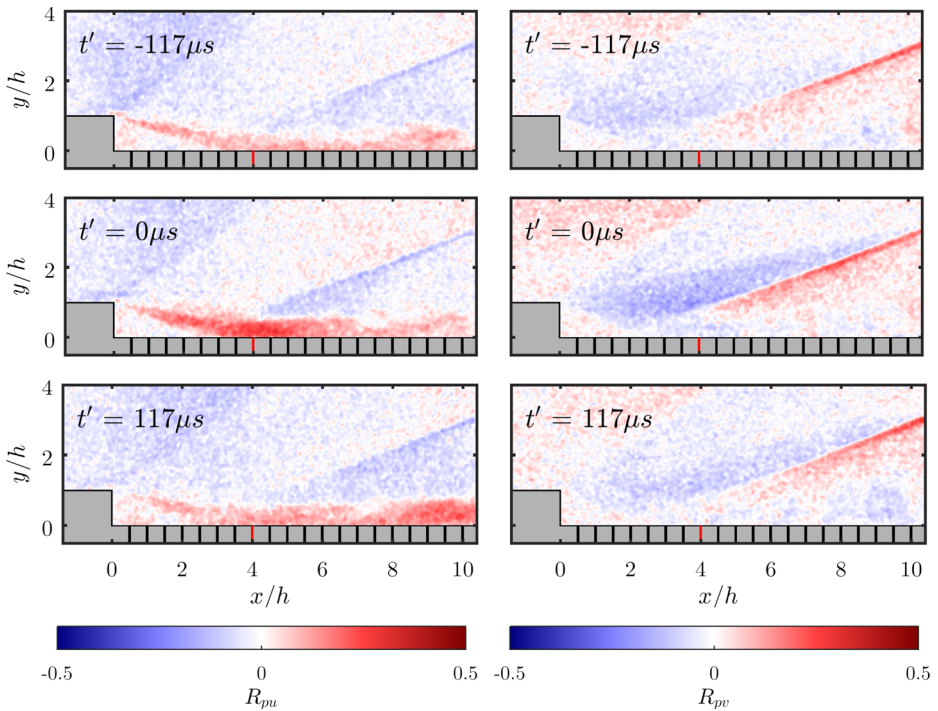


Fig. 15 Correlation of pressure fluctuations at $x/h = 4$ to the scalars of the velocity field fluctuations at $Ma_\infty = 2.0$. Left column shows R_{pu} , right column shows R_{pv} . Images from top to bottom are offset by two time steps of the pressure transducers or $t' = 117 \mu s$

The spectrum at $Ma_\infty = 2.0$ (refer to Fig. 13) shows a dominant peak around 1800 Hz, which is a natural frequency of the TWM as stated previously. At approximately $x/h = 4$, a broadband peak extends from above 1000 Hz to 4000 Hz ($Sr_h = 0.015 - 0.06$). This peak does not appear in the velocity/pressure correlations, as the pumping motion of the recirculation area occurs at substantially lower frequencies as seen in the spatial spectrum between 50 – 400 Hz, depending on the streamwise location.

Overall, for the supersonic regime, it can be concluded that the driving mechanism for the load fluctuations on the reattachment surface are vastly different than below sonic conditions. This could also be seen in Fig. 12, when tracking the pressure fluctuations in space and time, where the mechanism for the supersonic case is vastly different from the transonic one. The most dominant flow motion resolved with the combined PIV/pressure correlations is a low-frequency pumping motion of the recirculation area. This is good agreement with literature, where it is stated that this is caused by the dynamics of the separated bubble [44–46].

4 Summary and Conclusions

Experiments on a BFS in sub-, trans- and supersonic conditions have been carried out in order to determine the main mechanism for the most dominant pressure loads experienced by the reattachment surface, depending on the flow regime. Measurements were conducted

with PIV, dynamic pressure transducers, and a combination thereof. It was shown that the intensities of the normalized pressure fluctuations do not correlate with the intensities of the normalized Reynolds shear stresses between the various Mach numbers. However, the location and distribution of the Reynolds shear stresses close to the surface give a good indication of the distribution of p'_{RMS} .

The results clearly show that the dominant pressure fluctuations below sonic conditions are caused by Kelvin-Helmholtz instabilities in the form of the step mode, while in the supersonic regime a low-frequency pumping of the recirculation zone is the dominant motion. This indicates that the underlying physics governing flow separation and reattachment in sub- and supersonic flows are vastly different, and thus lead to distinct dynamics. The dynamic loads on the reattachment surface increase up to transonic conditions, however they drastically decrease once the flow aft of the BFS becomes locally supersonic. This leads the authors to believe that the pressure fluctuations occurring aft of a BFS in supersonic flow are more comparable to that of supersonic boundary layer pressure fluctuations. This is supported by the fact that for instance $p_{\text{RMS}}/q_{\infty}$ of 0.4 is nearly identical to that found in supersonic boundary layers at $Ma_{\infty} = 2.0$ [47]. Further supporting this hypothesis is the fact that the correlations clearly separate the areas of outer flow (assumed to be supersonic as explained in Section 3.7.2) from the recirculation region and the newly developing boundary layer (assumed to be below sonic conditions). This indicates that only the subsonic flow has an effect on the pressure loads on the surface. The fact that the supersonic flow above a boundary layer for instance, does not protrude into the subsonic regions is also one of the challenges of getting particles for PIV into boundary layers at supersonic flow conditions. Similarly, the fact that the locally sub- and supersonic regions do not mix, is one of the challenges in supersonic combustion.

The findings in this manuscript could be helpful for the design of future aerospace vessels that have to travel in- or through the transonic regime into the supersonic regime.

Acknowledgements Financial support from the German Research Foundation in the framework of the TRR40 – Technological foundations for the design of thermally and mechanically highly loaded components of future space transportation systems – is gratefully acknowledged by the authors.

Compliance with Ethical Standards

Conflict of interests The authors declare that they have no conflict of interest.

Publisher's Note Springer Nature remains neutral with regard to jurisdictional claims in published maps and institutional affiliations.

References

1. Statnikov, V., Bolgar, I., Scharnowski, S., Meinke, M., Kähler, C.J., Schröder, W.: Analysis of characteristic wake flow modes on a generic transonic backward-facing step configuration. *Eur. J. Mech. B. Fluids* **59**, 124–134 (2016)
2. Hannemann, K., Lüdeke, H., Pallegoix, J.-F., Ollivier, A., Lambar, H., Maseland, J.E.J., Geurts, E.G.M., Frey, M., Deck, S., Schrijer, F.F.J., Scarano, F., Schwane, R.: Launcher vehicle base buffeting - recent experimental and numerical investigations. In: *Proceedings 7th European symposium on aerothermodynamics for space vehicles*, Brugge (2011)
3. Scharnowski, S., Statnikov, V., Meinke, M., Schröder, W., Kähler, C.J.: Combined experimental and numerical investigation of a transonic space launcher wake. In: *Progress in flight physics*, vol. 7, pp. 311–328. EDP Sciences (2015)

4. Eaton, J.K., Johnston, J.P.: A Review of Research on Subsonic Turbulent Flow Reattachment. *AIAA J* **19**, 1093–1100 (1981)
5. Kuehn, D.M.: Effects of adverse pressure gradient on the incompressible reattaching flow over a Rearward-Facing step. *AIAA J* **18**(6), 343–344 (1980)
6. Isomoto, K., Honami, S.: The effect of inlet turbulence intensity on the reattachment process over Backward-Facing step. *J. Fluid Eng-T ASME* **111**, 87–92 (1989)
7. Bernard, N., Sujar-Garrido, P., Bonnet, J.-P., Moreau, E.: Control of the coherent structure dynamics downstream of a backward-facing step by dbd plasma actuator. *Int. J. Heat Fluid Flow* **61**, 158–173 (2016)
8. Hasan, M.A.Z.: The flow over a backward-facing step under controlled perturbation. *J. Fluid Mech.* **238**, 73–96 (1992)
9. Ho, C.-M., Huerre, P.: Petrubed free shear layers. *Ann. Rev. Fluid Mech.* **16**, 365–424 (1984)
10. Eaton, J.K., Johnston, J.P.: Turbulent flow reattachment: an experimental study of the flow and structure behind a backward-facing step. Technical report, Dept. of Mech. Eng. Stanford Univ (1980)
11. Cherry, N.J., Hillier, R., Latour, M.E.M.P.: Unsteady measurements in a separated and reattaching flow. *J. Fluid Mech.* **144**, 13–46 (1984)
12. Driver, D.M., Seegmiller, H.L., Marvin, J.G.: Time-dependent behavior of a reattaching shear layer. *AIAA J* **25**(7), 914–919 (1987)
13. Heenan, A.F., Morrison, J.F.: Passive control of pressure fluctuations generated by separated flow. *AIAA J* **36**(6), 1014–1025 (1998)
14. Lee, I., Sung, H.J.: Characteristics of wall pressure fluctuations in separated and reattaching flows over a backward-facing step. *Exp. Fluids* **30**, 262–272 (2001)
15. Scharnowski, S., Bolgar, I., Kähler, C.J.: Control of the recirculation region of a transonic backward-facing step flow using circular lobes. In: 9th Int. Symp. on turbulence and shear flow phenomena (TSFP-9), Melbourne (2015)
16. Scharnowski, S., Bolgar, I., Kähler, C.J.: Characterization of turbulent structures in a transonic backward-facing step flow. *Flow Turbul. Combust* (2016)
17. Barkley, D., Gomes, M.G.M., Henderson, R.D.: Three-dimensional instability in flow over a backward-facing step. *J. Fluid Mech.* **473**, 167–190 (2002)
18. Beaudoin, J.-F., Cadot, O., Aider, J.-L., Wesfreid, J.E.: Three-dimensional stationary flow over a backward-facing step. *Eur. J. Mech. B/Fluids* **23**(1), 147–155 (2004)
19. Ginoux, J.J.: Streamwise vortices in reattaching high-speed flows—a suggested approach. *AIAA J* **9**(4), 759–760 (1971)
20. Statnikov, V., Roidl, B., Meinke, M., Schröder, W.: Analysis of spatio-temporal wake modes of space launchers at transonic flow. In: 54th AIAA aerospace sciences meeting (2016)
21. Deck, S., Thorigny, P.: Unsteadiness of an axisymmetric separating-reattaching flow: Numerical investigation. *Phys. Fluids* **19**, 065103 (2007)
22. Halupovich, Y., Natan, B., Rom, J.: Numerical solution of the turbulent supersonic flow over a backward facing step. *Fluid Dyn. Res.* **24**, 251–273 (1999)
23. Roshko, A., Thomke, G.J.: Observations of turbulent reattachment behind an Axisymmetric downstream-facing step in supersonic flow. *AIAA J* **4**, 975–980 (1966)
24. de Brederode, V., Bradshaw, P.: Three-Dimensional Flow in Nominally Two-Dimensional Separation Bubbles: Flow Behind a Rearward-Facing Step. Technical Report, Imperial College, London, Great Britain (1972)
25. Kähler, C.J., Sammler, B., Kompenhans, J.: Generation and control of particle size distributions for optical velocity measurement techniques in fluid mechanics. *Exp. Fluids* **33**, 736–742 (2002)
26. Scharnowski, S., Kähler, C.J.: On the effect of curved streamlines on the accuracy of PIV vector fields. *Exp. Fluids* **54**, 1435 (2013)
27. Scharnowski, S., Kähler, C.J.: Estimation and optimization of loss-of-pair uncertainties based on PIV correlation functions. *Exp. Fluids* **57**, 23 (2016)
28. Mendez, M.A., Raiola, M., Masullo, A., Discetti, S., Ianiro, A., Theunissen, R., Buchlin, J.-M.: POD-Based background removal for particle image velocimetry. *Exp. Thermal Fluid Sci.* **80**, 181–192 (2017)
29. Avallone, F., Discetti, S., Astarita, T., Cardone, G.: Convergence enhancement of single-pixel PIV with symmetric double correlation. *Exp. Fluids* **56**(4), 1–11 (2015)
30. Kähler, C.J., Scharnowski, S., Cierpka, C.: On the resolution limit of digital particle image velocimetry. *Exp. Fluids* **52**, 1629–1639 (2012)
31. Bolgar, I., Scharnowski, S., Kähler, C.J.: Correlations between Turbulent Wall Pressure and Velocity Field Fluctuations in Backward-Facing Step Flows. Deutscher Luft- Und Raumfahrtkongress, Munich. Deutsche Gesellschaft für Luft- und Raumfahrt (2017)

32. Buchmann, N.A., Küçükosman, Y.C., Ehrenfried, K., Kähler, C.J.: Wall pressure signature in compressible turbulent boundary layers. *Progress in Wall Turbulence* **2**, 93–102 (2016)
33. Chovet, C., Lippert, M., Foucaut, J.M., Keirsbulck, L.: Dynamical aspects of a backward-facing step flow at large Reynolds numbers. *Exp. Fluids* **58**(11), 162 (2017)
34. Hudy, L.M., Naguib, A., Humphreys, W.M.: Stochastic estimation of a separated-flow field using wall-pressure-array measurements. *Phys. Fluids* **19**(2), 024103 (2007)
35. Rodgers, J.L., Nicewander, W.A.: Thirteen ways to look at the correlation coefficient. *Am. Stat.* **42**(1), 59–66 (1988)
36. Hampel, A.: Auslegung, Optimierung Und Erprobung Eines Vollautomatisch Arbeitenden Transsonik-Windkanals. Dissertation, Hochschule der Bundeswehr (1984)
37. Schlichting, H., Gersten, K.: *Grenzschicht-Theorie*. Springer, Berlin (2006)
38. Ross, C.B., Lourenco, L.M., Krothapalli, A.: Particle image velocimetry measurements in a shock-containing supersonic flow. *AIAA Paper*, (94–0047) (1994)
39. Ragni, D., Schrijer, F., Oudheusden, B.W., Scarano, F.: Particle tracer response across shocks measured by PIV. *Exp. Fluids* **50**, 53–64 (2011)
40. Scharnowski, S., Kähler, C.J.: Investigation of a transonic separating/reattaching shear layer by means of PIV. *Theor. Appl. Mech. Lett.* **5**, 30–34 (2015)
41. Depres, D., Reijasse, P., Dussauge, J.P.: Analysis of Unsteadiness in Afterbody Transonic Flows. *AIAA J* **42**, 2541–2550 (2004)
42. Le, H., Moin, P., Kim, J.: Direct numerical simulation of turbulent flow over a backward-facing step. *J. Fluid Mech.* **330**, 349–374 (1997)
43. Troutt, T.R., Scheelke, B., Norman, T.R.: Organized structures in a reattaching separated flow field. *J. Fluid Mech.* **143**, 413–427 (1984)
44. Dolling, D.S.: Fifty years of Shock-Wave/Boundary layer interaction research: What Next? *AIAA J* **39**(8), 1517–1531 (2001)
45. Kistler, A.L.: Fluctuating Wall Pressure under a Separated Supersonic Flow. *J. Acoust. Soc. Am.* **36**(3), 543–550 (1964)
46. Piponniau, S., Dussauge, J.P., Dèbieve, J.F., Dupont, P.: A simple model for low-frequency unsteadiness in shock-induced separation. *J. Fluid Mech.* **629**, 87–108 (2009)
47. Bernardini, M., Pirozzoli, S.: Wall pressure fluctuations beneath supersonic boundary layers. *Phys. Fluids* **23**, 1–11 (2011)